Radio Scintillations in Venus's Atmosphere: Application of a Theory of Gravity Wave Generation*

STEPHEN S. LEROY† AND ANDREW P. INGERSOLL

Division of Geological and Planetary Sciences, California Institute of Technology, Pasadena, California

(Manuscript received 2 February 1995, in final form 12 October 1995)

ABSTRACT

Radio scintillations in *Pioneer Venus* radio occultation data are simulated assuming that the index of refraction fluctuations in Venus's atmosphere responsible for the scintillations are directly caused by gravity wave fluctuations. The gravity waves are created by a global convection layer between 50- and 55-km altitude in Venus's atmosphere and propagate vertically. The authors compare the simulated scintillations with data from *Pioneer Venus*.

These gravity waves can explain the spectral shape and amplitude of the radio scintillations. The shape at high frequencies is controlled by wave breaking, which yields a saturated spectrum. The amplitude is subject to parameters such as the intensity of the convection, the angle between the zonal winds and the beam path, and the zonal wind profile at polar latitudes. To match the observed amplitude of the scintillations, the velocity variations of the energy-bearing eddies in the convection must be at least 2 m s^{-1}. This value is consistent with the Venus balloon results of Sagdeev et al. and is in the middle of the range considered by Leroy and Ingersoll in their study of convectively generated gravity waves. The latter study, combined with the lower bound on velocity from the present study, then yields lower bounds on the vertical fluxes of momentum and energy in the Venus atmosphere.

1. Introduction

In a previous theoretical paper we investigated whether gravity waves generated by global-scale convection in Venus's middle atmosphere could support the westward superrotation (Leroy and Ingersoll 1995, LI1 hereafter). We found that the waves carry enough momentum to support the superrotation but that the distribution of accelerations in altitude is unsatisfactory. We also found that the waves transport large amounts of eastward momentum to great heights, where the waves might dominate the mean motion as gravity waves are thought to do in the earth's mesosphere. Here we implement the gravity wave spectrum of LI1 in simulations of radio scintillations and compare our results with radio scintillation data of *Pioneer Venus*. Recently, similar scintillations were observed by *Magellan* (Jenkins and Steffes 1994) and shown to be consistent with vertically propagating internal gravity waves (Hinson and Jenkins 1995), but the source and amplitude for the waves has not been identified with certainty. Our goal is to check the theory of LI1 by verifying that convectively generated gravity waves are present in the Venus middle atmosphere.

Radio scintillations occur when the beam path of the *Pioneer Venus* radio signal passes through the Venus atmosphere on its course to earth (Kliore and Patel 1980). During the occultation, the *Pioneer Venus* spacecraft appears, to a terrestrial observer, to be moving vertically in the Venus atmosphere. The amplitude and phase (in the form of frequency shifts) of the radio signal are obtained as a function of time during the occultation. Because the density of the atmosphere is the primary source of refractive index variations, the data can be directly inverted to give vertical profiles of temperature but only at vertical resolutions greater than the width of the radio beam in the Venus atmosphere (Fjeldbo et al. 1971). Variations on scales smaller than the beamwidth can lead to amplitude and phase variations that cannot be directly inverted but can be statistically modeled (Tatarskii 1961). These variations in amplitude and phase are radio scintillations.

We use the same numerical technique as Woo and Armstrong (1980, WA hereafter) for simulating radio scintillations, but we assume that the density inhomogeneities are the fluctuations of internal gravity waves generated by convection in the Venus middle atmo-

* Contribution Number 5503 of the Division of Geological and Planetary Sciences of the California Institute of Technology.

† Current affiliation: Earth and Space Sciences Division, Jet Propulsion Laboratory, California Institute of Technology, Pasadena, California.

Corresponding author address: Dr. Stephen S. Leroy, Earth and Space Sciences Division, Jet Propulsion Laboratory, 183-335, California Institute of Technology, 4800 Oak Grove Dr., Pasadena, CA 91109.

sphere. We choose this as the most probable source for the density variations because the convection is nearly global in scale and is situated in a 5-km thick layer between the stable layers at 45- and 60-km altitude. The source is required to be global in scale because the scintillations in the *Pioneer Venus* radio science were found to be global. Scintillations were also seen near 60 km by *Mariner 5* (Woo et al. 1974), *Mariner 10* (Woo 1975), and *Venera 9* (Timofeeva et al. 1978). We choose gravity waves because they can propagate over large vertical distances and they can have structure on small vertical scales. With such criteria, therefore, we presume that gravity waves generated by the convection in the Venus middle atmosphere are a probable creator of the scintillations in *Pioneer Venus* radio science data.

The motion of the spacecraft carries the beam rapidly through the atmosphere. The enhanced scintillations seen at 60 km are apparent primarily in a window of about 10 s, corresponding to an altitude range of about 10 km. The timescale for atmospheric motions is several minutes (the inverse of the Brunt–Väisälä frequency). Thus, we use the "frozen-in" hypothesis, which postulates that the density variations are frozen in the atmosphere and exist only as a function of space where the occultation experiment is concerned.

In LI1, the convecting layer was placed between 50- and 55-km altitude. Just above the convection, the atmosphere is statically stable, with the square of the Brunt–Väisälä frequency given by $N_c^2 = 4 \times 10^{-5}\ \mathrm{s}^{-2}$. The stability increases with altitude to about $N^2 = 3.6 \times 10^{-4}\ \mathrm{s}^{-2}$ at 60-km altitude. The atmosphere is statically stable below the convection as well, but we restrict ourselves to analysis of the overlying stable atmosphere. The winds are westward and increase by about 55 m s^{-1} between the convection and 67-km altitude. There is no shear or static stability within the convection itself. LI1 used WKBJ theory to relate the amplitude and spectrum of convective eddies to the amplitude and spectrum of gravity waves in the stable layer above the convection. An important parameter in LI1 is U_c, the magnitude of the velocity variations in the convection. The present analysis gives a lower bound on U_c and thus a lower bound on the energy and momentum fluxes derived from the LI1 theory.

Prominent in the results of LI1 are two types of wave breaking: *breaking upon emission* from the convection and *critical layer breaking* near critical layers. Immediately upon emission from the convection, low frequency, and, hence, low phase speed, waves were found to be convectively unstable. Accordingly, we decreased the amplitude of the waves within each unit logarithmic band of vertical wavenumber ($\delta m/m \sim 1$) to the point where the waves are marginally stable. This led to a saturated spectrum proportional to m^{-3} (Dewan and Good 1986; Smith et al. 1987). In addition, the presence of a shearing zonal wind created critical layers, near which gravity waves become unstable via both Kelvin–Helmholtz and convective instabilities (Geller et al. 1975). Again, we decreased the amplitude of the waves such that the waves are marginally stable. As shown below, the waves that remain after breaking are sufficient to cause the observed scintillations.

2. Gravity waves as a source of radio scintillations

a. The scintillation integral

In the theory of scintillations in radio occultations using the Rytov approximation (Tatarski 1961; Ishimaru 1973, 1978), one of the important quantities is χ, the logarithm of the electric field of the radio signal as viewed from earth. Since χ can be quantified only in a statistical sense, we analyze the variance spectrum of χ in frequency. This log-amplitude variance spectrum $W_\chi(\nu)$ is defined as

$$W_\chi(\nu) \equiv 2 \int_{-\infty}^{\infty} d\Delta t\, \overline{\chi(t)\chi(t+\Delta t)} \cos 2\pi\nu\Delta t. \tag{1}$$

Haugstad (1979) and Woo et al. (1980b) show how this is related to the refractive index variance spectrum through

$$W_\chi(\nu) = 4\pi^2 k^2 L \int dk_y'\, dm\, \mathbf{B}_{n_1}(k_x' = 0, k_y', m) \times \sin^2\left[a_f^2\left(k_y'^2 + \frac{m^2}{q^2}\right)\right][\delta(2\pi\nu - k_y'\dot{y}_a - m\dot{z}_a) + \delta(2\pi\nu + k_y'\dot{y}_a + m\dot{z}_a)]. \tag{2}$$

Here, ν is the frequency, k is the free-space wavenumber of the radio signal, $B_{n_1}(k_x', k_y', m)$ is the variance spectrum of refractive index fluctuations in the spatial wavenumbers (k_x', k_y', m), where k_x' and k_y' are the horizontal wavenumbers in Venus's atmosphere tangent to and transverse to the radio beam path, m is the vertical wavenumber, $\dot{y}_a$ and $\dot{z}_a$ are the apparent spacecraft motions in the horizontal and vertical directions on Venus, and x' is the distance coordinate along the line of sight to the spacecraft. The horizontal Fresnel size a_f is given by $(R/2k)^{-1/2}$. The quantity R is the radius of curvature and is given by

$$\frac{1}{R} = \frac{1}{R_1} + \frac{1}{R_2},$$

where R_1 is the distance from the spacecraft to the occulting atmosphere and R_2 is the distance from the occulting atmosphere to the observer (at earth). The defocusing factor q^2 is the factor by which the radio signal is spread out by refraction in Venus's atmosphere ($q^2 = 10$ for the case considered here). The apparent velocity of the spacecraft, given by $\dot{y}_a$ and $\dot{z}_a$, is the velocity of the spacecraft as it appears to the observer, including the effect of refraction. That is, $\dot{y}_a = \dot{y}_s$ and

$\dot{z}_a = \dot{z}_s/q^2$, where $\dot{y}_s$ and $\dot{z}_s$ are the actual spacecraft velocity components (Haugstad 1979, p. 329; Woo et al. 1980, p. 697). Each wave mode contributes at a frequency given by the rate at which the spacecraft crosses the mode's phase fronts, as required by the Dirac delta functions $\delta(\cdots)$. Averaging along the beam path guarantees that only waves with $k_x' = 0$ contribute to the variance of χ.

Most of the scintillations are due to vertical motion of the beam through the atmosphere, so there is nearly a one to one correspondence between frequency ν and vertical wavenumber m. This is because the $m\dot{z}_a$ term is larger than the $k_y'\dot{y}_a$ term in the Dirac delta functions when the integrand is largest. The biggest contributors to the scintillations have $k_y' \leqslant 1/H$, where H is approximately a scale height, which is in turn approximately the horizontal scale of the energy-bearing eddies in the convection. There is no restriction on m, however, since $m \to \infty$ as the waves approach critical layers. Only those waves with $a_f m/q \geqslant 1$ will contribute significantly to the scintillations, because only then is the argument of the sine term in (2) greater than unity. (The upper bound on k_y' ensures that it does not contribute significantly to the argument of the sine term.) Thus, $|(m\dot{z}_a)/(k_y'\dot{y}_a)| \geqslant (qH/a_f)|\dot{z}_a/\dot{y}_a|$ in which $qH/a_f = 80$ for $q^2 = 10$, $H = 5$ km, and $a_f = 200$ m. Given that the actual spacecraft motion is related to the apparent spacecraft motion through $\dot{y}_a = \dot{y}_s$ and $\dot{z}_a = \dot{z}_s/q^2$, the lower bound on the ratio of $m\dot{z}_a$ to $k_y'\dot{y}_a$ becomes $8|\dot{z}_s/\dot{y}_s|$. Since this lower bound is much greater than unity for most spacecraft motions, the $m\dot{z}_a$ term is much greater than the $k_y'\dot{y}_a$ term; hence, the vertical wavenumber m determines the frequency ν.

Equation (2) differs from Eq. (2.5) of Haugstad (1979) [cf. Eq. (8) of Woo et al. (1980)] only in that we have two Dirac delta functions and they have one. When implementing turbulence, only one delta function is necessary, as long as an extra factor of 2 is included, because the spectrum of turbulence is symmetric about $k_y' = 0$. For gravity waves in a shear flow, however, such a symmetry is not expected; thus, we must retain both delta functions.

We implement gravity waves in (2) by introducing polar coordinates in the plane transverse to the beam path in Venus's atmosphere. We set

$$k_y' = \kappa \sin\theta, \quad m = \kappa \cos\theta, \tag{3}$$

where κ is the amplitude of the wave vector in the y', z' plane and θ is the angle away from the vertical at which a wave mode propagates. For consistency, we rewrite the apparent spacecraft velocity $\dot{y}_a$, $\dot{z}_a$ in polar coordinates:

$$\dot{y}_a = v_a \sin\alpha, \quad \dot{z}_a = v_a \cos\alpha, \tag{4}$$

where v_a is the apparent speed of the spacecraft and α is the angle away from the vertical at which the spacecraft appears to travel. When we insert the above expressions into (2), the integration is over κ and θ. The delta functions allow us to integrate over κ. This leaves

$$W_\chi(\nu) = 8\pi^2 k^2 L \frac{2\pi\nu}{v_a^2} \int_{\alpha-\pi/2}^{\alpha+\pi/2} d\theta \sec^2(\theta-\alpha) \sin^2\left[\frac{2\pi^2\nu^2 R}{k v_a^2} \sec^2(\theta-\alpha)\left(\sin^2\theta + \frac{\cos^2\theta}{q^2}\right)\right]$$
$$\times \left\{ \mathbf{B}_{n_1}\left[k_x' = 0, k_y' = \frac{2\pi\nu}{v_a}\sec(\theta-\alpha)\sin\theta, m = \frac{2\pi\nu}{v_a}\sec(\theta-\alpha)\cos\theta\right] \right.$$
$$\left. + \mathbf{B}_{n_1}\left[k_x' = 0, k_y' = -\frac{2\pi\nu}{v_a}\sec(\theta-\alpha)\sin\theta, m = -\frac{2\pi\nu}{v_a}\sec(\theta-\alpha)\cos\theta\right]\right\}. \tag{5}$$

The power spectrum in this equation is the same as that in Eq. (2) except that the three arguments k_x', k_y', m of the index refraction spectrum are determined by the frequency ν, the apparent spacecraft speed v_a, the apparent spacecraft entry angle α, and the angle θ.

The x', y' coordinates are defined relative to the line of sight to the spacecraft. The horizontal wavenumber pair k_x, k_y is defined relative to the mean wind, with x in the direction of the wind and y transverse to it. This is the coordinate system used by LI1. To transform to the x', y' system used for analyzing scintillations, we rotate through an angle Δ. When the mean wind is in the zonal direction, Δ is the angle between the radio beam path and a line of constant latitude at the beam's closest approach to the planet's surface. Then the angle Δ is related to the obliquity B of the planet to earth and the latitude λ of the occultation through

$$\sin\Delta = \frac{\sin B}{\cos\lambda}. \tag{6}$$

b. Index of refraction fluctuations

As mentioned earlier, the index of refraction fluctuations n_1 are related to the density fluctuations in the atmosphere. We use the first law of thermodynamics and (4) of LI1 to show that

$$\frac{\rho'}{\bar{\rho}} = \frac{\phi'}{\gamma RT} - \frac{S'}{c_p}, \quad (7)$$

where ρ' is the density fluctuation, ϕ' is the pressure fluctuation divided by the mean density $\bar{\rho}$, S' is the specific entropy fluctuation, γ is the adiabatic index, and c_p is the specific heat at constant pressure. To compare the two terms on the right-hand side of this equation, we solve for S' in terms of ϕ':

$$S' = \frac{c_p}{g_v} \frac{N^2}{N^2 - \tilde{\omega}^2} \frac{\partial \phi'}{\partial z}, \quad (8)$$

where N is the Brunt–Väisälä frequency, g_v is Venus's gravitational acceleration, $\tilde{\omega} = k_x[c_x - \bar{u}(z)]$ is the wind-shifted frequency of the wave, and m is the vertical wavenumber. The notation and derivation are the same as in LI1. The square of the vertical wavenumber is given as

$$m^2 = \frac{N^2 - \tilde{\omega}^2}{\tilde{\omega}^2} k^2, \quad (9)$$

where k is the horizontal wavenumber [given by $(k_x^2 + k_y^2)^{1/2}$]. When the WKBJ approximation is valid such that $mH \gg 1$, the second term, which is proportional to the entropy fluctuation, dominates the first term, which is proportional to the pressure fluctuation, on the right in (7). Using the above expression for the entropy fluctuation, the density fluctuation ρ' can be written as a function of ϕ':

$$\rho' \approx -\frac{\bar{\rho}(z)}{g_v} \frac{N^2}{N^2 - \tilde{\omega}^2} \frac{\partial \phi'}{\partial z}. \quad (10)$$

Several authors have calculated the coefficient relating density fluctuations and refractive index fluctuations for Venus's atmosphere (Essen and Froome 1951; Woo 1975). We use the value given by WA, which is

$$n_1 = (1.35 \times 10^{-6}\ \mathrm{K\ Pa^{-1}}) R_g \rho', \quad (11)$$

in which R_g is the gas constant for Venus's atmosphere, $R_g = 189.0\ \mathrm{J\ kg^{-1}\ K^{-1}}$ (Seiff et al. 1980).

With the two preceding equations and Eq. (27) of LI1, we can write the power spectrum of index of refraction fluctuations as

$$\mathbf{B}_{n_1}(k_x, k_y, m) = (2.55 \times 10^{-4}\ \mathrm{m^3\ kg^{-1}})^2 \left[\frac{\bar{\rho}(z)}{g_v}\right]^2 \times \frac{N^4}{(N^2 - \tilde{\omega}^2)^2} \left|\frac{\partial h}{\partial z}\right|^2 M(k_x, k_y, m). \quad (12)$$

Following LI1, we use $h(z)$ to represent a normalized form of the ρ' fluctuation in the region above the convection, and M to represent the wave response to forcing by the convection. We evaluate M differently depending on whether a particular wave mode, determined by k_x, k_y, and m, radiates to space or propagates strictly horizontally.

For waves that radiate to space (*propagating* waves), $M(\omega, k_x, k_y)$ is given by equation (32) of LI1. One transforms to $M(k_x, k_y, m; z)$ using

$$M(k_x, k_y, m; z) = \left|\frac{\partial \omega}{\partial m}\right|_{k_x, k_y, z} M(\omega, k_x, k_y). \quad (13)$$

The quantity $\mathcal{C}$ in Eq. (32) of LI1 is given by Eq. (18) of LI1.

For waves restricted to horizontal propagation (*trapped* waves), LI1 do not give an expression for M because these waves do not contribute to vertical momentum transport. In this paper we must consider their amplitude because they do cause refractive index fluctuations. Trapped waves contribute much of their amplitude resonantly. This could be problematic because these resonances can be thinner spectrally than the interval we choose for spectral integration; however, by analytically integrating over the resonances, as shown in the next section, we can account for all of the amplitude.

c. *Trapped wave amplitudes*

Here we find an analytic expression for the amplitude contained in a resonantly trapped gravity wave. In LI1 we used a model atmosphere in which the square of the Brunt–Väisälä frequency was zero inside the convection and was N_c^2 immediately above the convection, with $N_c^2 \approx 4 \times 10^{-5}\ \mathrm{s^{-2}}$. The energy-bearing eddies have length scales $1/k$ of order 5 km and velocity variations U_c of order 3 m s^{-1}. The corresponding frequencies ($\omega = kU_c \approx 6 \times 10^{-4}\ \mathrm{s^{-1}}$), are smaller than N_c, so we assume that $\omega \ll N_c$. The results of this section do not depend on the size of ω compared to N_c, but calculating the overall contribution of resonances is most easily done in the small frequency limit.

According to (32) of LI1, M is inversely proportional to $|\mathrm{Wr}|^2$, where $\mathrm{Wr}(g, h)$ is the Wronskian of the two independent solutions $g(z)$ and $h(z)$. The former satisfies the lower boundary condition at the base of the convection; the latter satisfies the upper boundary condition above the convection. LI1 consider propagating waves. However, $h(z)$ for trapped waves is different from $h(z)$ for propagating waves. This affects the expression for the Wronskian. Trapped waves are those that are confined to a horizontal layer or duct. Since $N^2 = 0$ within the convection and $N^2 = N_c^2$ immediately above the convection, the top of the convection layer is the lower boundary of the duct. The upper boundary of the duct is formed where the Doppler-shifted frequency $\tilde{\omega}$ exceeds $N(z)$ and m^2 becomes negative. The form of $h(z)$ within the duct is

$$h(z) \approx \tilde{\omega} \sqrt{\frac{|m|}{\bar{\rho}}} \sin(Q_d - p - \pi/4),$$

where the phase p is measured from the top of the convecting layer and the phase Q_d is the total phase within

the duct. Evaluating h and $\partial h/\partial z$ just above the convecting layer (where $p = 0$) and substituting into Eq. (14) of LI1 gives

$$\mathrm{Wr}(g, h) = \omega k \sqrt{\frac{m_c}{\rho_c}} \left[\left(1 - \frac{i}{\omega \tau_c}\right) \frac{k}{m_c} \cos(Q_d - \pi/4) - \tanh kH \sin(Q_d - \pi/4) \right],$$

where ρ_c is the atmospheric density at the top of the convection. Since $\omega \ll N_c$, then $m_c \gg k$ [cf. Eq. (9)], and the first term in the square brackets is usually much less than the second. The second term becomes smaller than the first, however, when $Q_d \approx (n + 1/4)\pi$. In this region M is maximized and a resonance occurs. Since we anticipate that most of the amplitude contributed by trapped waves is done by resonant modes, we approximate M in the vicinity of a resonance. In doing so we define $\delta Q \equiv Q_d - (n + 1/4)\pi$ and expand $\sin(Q_d - \pi/4)$ and $\cos(Q_d - \pi/4)$ in δQ. After substituting $\delta Q \equiv \delta Q' + k/(m_c \tanh kH)$ and squaring the Wronskian, we find

$$|\mathrm{Wr}(g, h)|^2 = \frac{\omega^2 k^2 m_c}{\rho_c} \left[\frac{k^2}{\omega^2 \tau_c^2 m_c^2} + \tanh^2 kH (\delta Q')^2 \right]. \quad (14)$$

This expression appears in the denominator for the temperature variance [Eq. (32) of LI1]. Thus, each resonance has a Lorentzian line shape in $\delta Q'$ with a half-width at half-maximum of

$$\delta Q_L = \frac{k}{\omega \tau_c m_c \tanh kH}.$$

Note that the width of the resonance is inversely proportional to the damping timescale τ_c of the convection.

If we integrate M over this resonance with the variable of integration Q_d, we find how much amplitude the resonance will contribute to wave fluctuation variances. Furthermore, if we then divide by π, because each resonance is separated by π radians in the phase Q_d, we can find a "smooth" spectrum for trapped waves. This smooth spectrum is

$$M_{\mathrm{smooth}}(\omega, k_x, k_y) = \frac{\rho_c}{\omega^2 k^3} \frac{\omega \tau_c}{\tanh kH} \mathcal{C}(\omega, k_x, k_y). \quad (15)$$

We use this expression for M in evaluating the amplitude contributed by trapped waves in (12).

Even though the smooth spectrum for trapped waves was found by assuming $k \ll m_c$, it works well in many other limits. [See Leroy (1994) for some of these other limits.] In Fig. 1 we show a comparison between M and M_{smooth}. This figure shows that the smooth spectrum eliminates the resonances but preserves the overall integrated amplitude contributed by trapped waves.

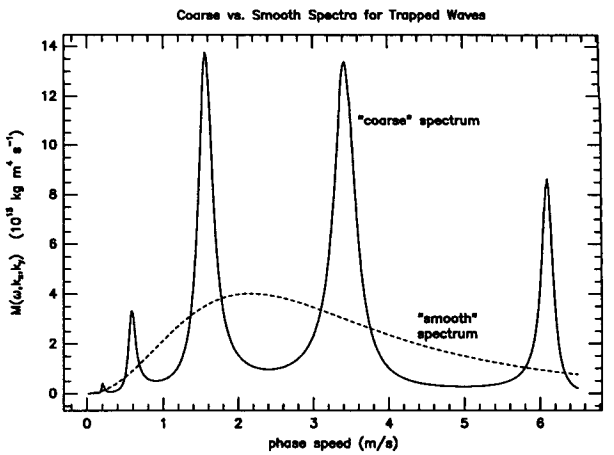

FIG. 1. Resonances in the wave response. We show $M(\omega, k_x, k_y)$ of Eq. (27) of LI1 (the "coarse" spectrum) and $M_{\mathrm{smooth}}(\omega, k_x, k_y)$ of (15) (the "smooth" spectrum). Both k and α are held fixed at 10^{-3} m^{-1} and 60° while c is varied. We use $U_c = 3$ m s^{-1} and $H_c = 5$ km.

We conclude the section by summarizing how one simulates log-amplitude radio scintillation spectra, given a gravity wave spectrum. The simulation equation is (5). We implement convectively generated gravity waves through (12), (13), and (15), where Δ is given by Eq. (6). The factor $M(\omega, k_x, k_y)$ is calculated using Eq. (32) of LI1, and $\partial h/\partial z$ is calculated as described in appendix B of LI1. Values for the parameters v_a, α, q^2, and Δ are different for each occultation.

3. Scintillation simulations

a. Scintillation data

For the sake of comparison, we reproduce the power spectrum of log-amplitude fluctuations at 60-km altitude in the S-band originally calculated by WA. Since this data is archived on outdated media and since only one spectrum was published, we digitized the data presented in Fig. 4 of WA (with their permission). The occultation is taken from orbit 18, day of year 356, 1978. It occurred at 86.6°N. It is hard to avoid high latitudes for *Pioneer Venus* occultations because the spacecraft was a polar orbiter.

We compute the power spectrum of log-amplitude variance from the digitized data. We fast Fourier transformed the data, squared each coefficient, and multiplied by 13.24 s, twice the time interval of the data. The factor of 2 enters because we fold negative frequencies in with positive frequencies. The digitized data and the power spectrum is presented in Fig. 2. We find that the total variance $\sigma_\chi^2 \approx 0.044$ is in agreement with WA, and thus the scintillations can be considered weak because $\sigma_\chi^2 \ll 1$.

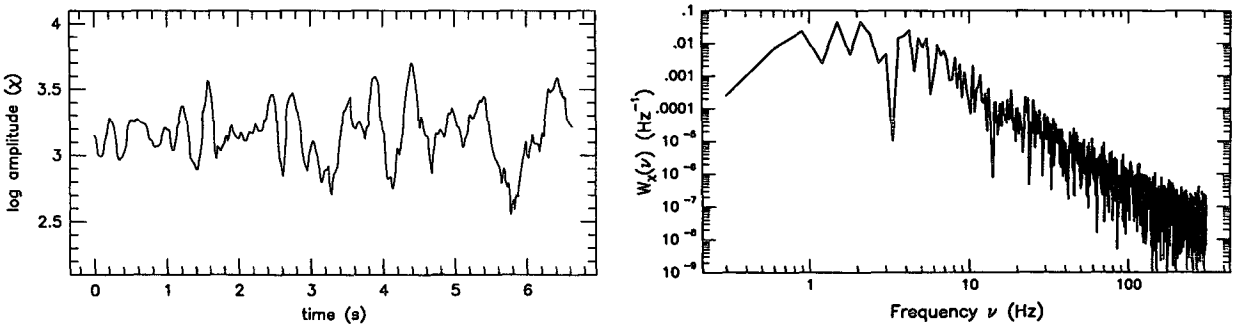

FIG. 2. The S-band scintillation data. (a) A reproduction of the S-band radio scintillation data presented by WA. The log of the field strength is plotted versus elapsed time during the occultation. This segment is centered at 60-km altitude in Venus's atmosphere. (b) The power spectrum of the data in panel a.

In our simulations, we intend to match the general trend of the power spectrum in the frequency interval between about 3 and 150 Hz. Power at frequencies below 3 Hz is not contributed by diffraction effects, because such low frequencies correspond to scales larger than the Fresnel size in Venus's atmosphere. The spectrum appears coarse above 3 Hz, which is the consequence of a single realization of a random process. With more realizations one could obtain a smoother spectrum by forming an ensemble average. The trend of the power spectrum changes slightly for frequencies greater than 150 Hz. At frequencies greater than about 100 Hz, several noise sources become important, including errors in our digitization.

Many parameters are explicitly determined by the geometry of the occultation in question. The spacecraft trajectory and defocusing factor determine the entry velocities $\dot{y}_a$ and $\dot{z}_a$. Woo and Armstrong (1980) give $v_s = 7.7$ km s^{-1} as the spacecraft motion without the effects of defocusing, and we have measured the spacecraft trajectory to be about 35° away from the vertical before it entered the atmosphere from Fig. 1 of Kliore and Patel (1980). Thus, $\dot{y}_s/\dot{z}_s = \tan 35°$. Since this is much less than 8 (see discussion in section 3a), the occultation can be considered vertical. Following WA we use $q^2 = 10$ at $z = 60$ km. Then the apparent motion of the spacecraft, including the effects of defocusing, are $\dot{y}_a = 7.7$ km s^{-1} $\times \sin 35° = 4.42$ km s^{-1} and $\dot{z}_a = 7.7$ km s^{-1} $\cos 35°/q^2 = 0.63$ km s^{-1}. This makes the apparent entry angle $\alpha = \tan^{-1}(\dot{y}_a/\dot{z}_a) = 82°$ and the apparent entry velocity $v_a = 4.46$ km s^{-1}. Other determined parameters are the spacecraft to limb distance ($R_1 = 3819$ km) and the Venus–Earth distance ($R_2 = 69.9 \times 10^6$ km). Because $R_1 \ll R_2$, then $R \approx 3819$ km. Also, we use the S-band occultation data; thus the carrier frequency is $k = 48.2$ m^{-1}. The Fresnel size a_f is 200 m. The Fresnel size is the same as the beamwidth multiplied by π. Finally, we approximate the beam pathlength through the atmosphere as $L \approx (8R_{\text{Venus}}H)^{1/2}$, where R_{Venus} is the radius of Venus and H is a scale height in the atmosphere (see Fig. 7 in Woo et al. 1974). Using 6050 km as the radius of Venus and 5 km as the scale height, we find $L \approx 540$ km. This is consistent with WA.

b. *Simulations*

In this section we compare our computed radio scintillation spectra with the data. The two most sensitive parameters are the angle Δ between the radio beam path and the mean winds and the amplitude U_c of velocity fluctuations in the convection. Although the geometry of the occultation is known, the mean wind direction is not, particularly at the high latitudes where the occultations occur. Moreover, the resulting spectra are most sensitive to values of Δ around zero, the value if the mean winds are zonal, because then the occultation samples those special waves that do not interact with the mean winds. Many of the waves are absorbed in critical layers before they reach 60-km altitude, to which our data refer. The velocity amplitude U_c of the convection therefore affects the amplitude of the scintillations, because a greater fraction of the waves can propagate to 60-km altitude when U_c is large. Also, above a certain value of U_c, the wave emission from the convection is large enough so that the spectrum saturates throughout the frequency range of interest (about 2 Hz through 50 Hz). Since the observed spectrum shows evidence of saturation throughout this frequency range, we can at least derive a lower bound on the velocity amplitude U_c.

1) DEPENDENCE ON Δ

In exploring the dependence of $W_\chi(\nu)$ on Δ, we first set the entry angle α to zero so the occultation is purely vertical. The parameters v_s and q^2 remain 7.7 km s^{-1} and 10. The Fresnel size a_f is still 200 m. In Fig. 3a, we set the convective wind speed at $U_c = 1$ m s^{-1}, we implement the complete breaking of waves as described in section 2 of LI1, and we vary Δ from 0° to 40°. The spectra were determined at 60-km altitude. When $\Delta = 0°$, the beam path and the mean winds are parallel ($k_x = k_x'$). Since averaging over the beam path permits contributions only from waves with $k_x' = 0$,

only purely meridionally propagating waves are sampled ($k_x = 0$). Such waves experience no Doppler shifting because $\tilde{\omega} = \omega - k_x\bar{u} = \omega$. As Δ is increased, Doppler shifting does occur and gravity wave critical layers (i.e., altitudes at which $\tilde{\omega} = 0$) enter into the scintillation integral. Since waves are absorbed at their critical layers, much of the wave amplitude is lost below 60-km altitude for substantial values of Δ.

Figure 3 shows that the slope of the high-frequency part of the spectrum changes when Δ is near zero. The following is a heuristic argument to explain these changes. When Δ is near zero the wave modes sensed in these spectra are broken twice—first as they are emitted from the convection and second at 60-km altitude. According to (9), the waves with high m—those subject to breaking—tend to have low ω. For Δ near zero, the waves that contribute to the scintillations are not Doppler shifted. Waves with high m/low ω at 60 km also have high m/low ω at the top of the convection, where they break as discussed earlier. Further breaking of the high m/low ω waves occurs at higher altitude, as other waves, propagating in different directions relative to the mean flow, approach their critical layers. As we have formulated it, breaking reduces the amplitude of all waves within a given band of m, even if only some of the waves in the band are approaching critical layers. Each stage of breaking causes the spectrum to fall off more rapidly with m, so the scintillation spectra at low Δ have a steeper falloff with m (and hence with ν) than those where Δ is large.

As the angle Δ increases, Doppler shifting becomes more important. Large vertical wavenumbers at 60 km no longer imply large m just above the convection since $\tilde{\omega}$ now varies with height [see (9)]. Therefore, the amplitude of these waves is not affected by breaking upon emission. The amplitude of these waves is affected by breaking near critical layers, though. The effect is that the waves are marginally stable, and their temperature variance spectrum is just the saturated spectrum. Thus, the scintillation simulations with substantial Δ resemble the saturated spectrum of breaking gravity waves.

As can be seen in Fig. 3b, $W_\chi(\nu)$ steadily makes a transition from a very steep slope (approximately ν^{-5}) to a much shallower slope (approximately ν^{-3}). We evaluate when that transition is complete by determining when the Doppler shifting $k_x\bar{u}$ (where $\bar{u}$ is the difference in the mean wind between the convection and 60 km) is comparable to the frequency ω of the largest waves. Since $k_x = k_y' \sin\Delta$ (recall that $k_x' = 0$) and since the largest waves have $k \approx 1/H$, then $k_x \approx (1/H)\sin\Delta$. The frequency ω of the dominant waves is approximately U_c/H. Thus, the transition to a ν^{-2} dependence for $W_\chi(\nu)$ occurs when $\sin\Delta \approx U_c/\bar{u}$, where $\bar{u}$ is the difference in the zonal wind speed between 55- and 60-km altitude. For $U_c = 1$ m s^{-1} and $\bar{u} = 30$ m s^{-1}, this transition occurs at $\Delta \approx 2°$, which is close to what is seen in Fig. 3.

As Δ is increased even more, the simulated scintillation spectra retain the same dependence on ν but the overall amplitude falls (see Fig. 3a). This is because the westward energy-bearing waves are critically absorbed before they reach 60-km altitude and cannot contribute to the spectrum at 60 km. Waves are absorbed at their critical layers, which occur when $c = \bar{u}\sin\Delta$, where c is the horizontal phase speed. Since $\bar{u}$ increases from 0 to 30 m s^{-1} from the convection to 60-km altitude, all those waves with c less than $30\sin\Delta$ m s^{-1} are absorbed. This effect can be seen in Fig. 3a.

For a given U_c and given ν in the high-frequency range, the spectrum first increases with respect to Δ and then decreases. The increase occurs as the power-law becomes shallower at small Δ. The decrease occurs as more and more of the waves are critically absorbed below 60 km, when Δ is larger than $\sin^{-1}(U_c/\bar{u})$. Thus, for every value of U_c and ν, there exists a maximum in the amplitude of $W_\chi(\nu)$ with respect to Δ.

In this section we have found that, except for a small window around $\Delta \approx 0°$, most simulated scintillation spectra obey a ν^{-3} power law. The ν^{-3} spectrum shows the effects of the saturated spectrum of gravity waves, which arises because high vertical wavenumber waves break as they propagate vertically. See LI1 for a further

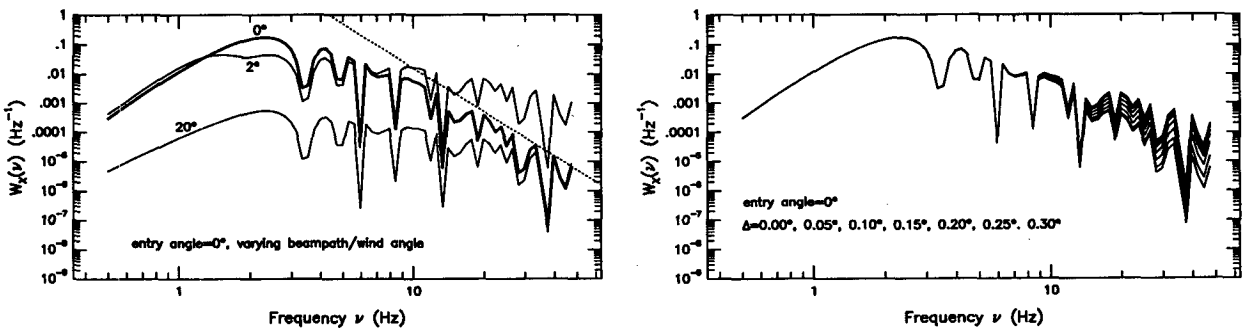

FIG. 3. Simulated scintillation spectra. Gravity waves are assumed responsible for the index of refraction fluctuations. The ordinate is the power spectrum of log-amplitude fluctuations. The gravity wave spectrum has $U_c = 1$ m s^{-1} and $H_c = 5$ km. The entry angle is set to 0°. (a) The angle Δ is set to 0° (bold curve), 2°, and 20° in succession. A dotted line with a slope of −5 is depicted. (b) The angle Δ varies from 0.0° to 0.3° in steps of 0.05°.

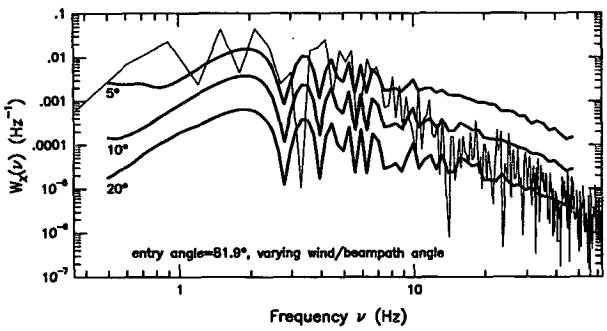

FIG. 4. Simulated scintillation spectra. The actual entry angle is 35°; the apparent entry angle is 81.9°. The gravity wave spectrum has $U_c = 1$ m s^{-1} and $H_c = 5$ km. The angle Δ is set to 10°, 20°, and 40°. The deemphasized curve is the data.

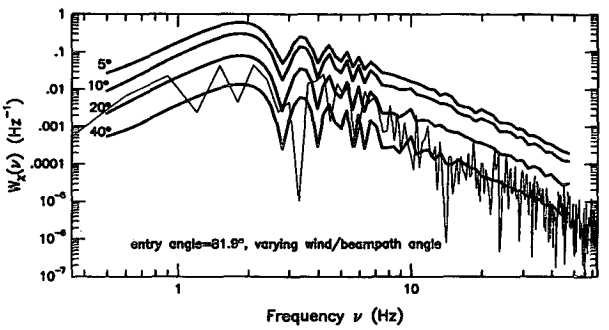

FIG. 5. Simulated scintillation spectra. The same as Fig. 4 but with $U_c = 3$ m s^{-1}. The angle Δ is set to 5°, 10°, 20°, and 40°.

discussion of the saturated spectrum and the ν^{-3} dependence.

2) DEPENDENCE ON U_c

Hereafter, we use a realistic entry angle (angle between the spacecraft motion and the atmospheric vertical) for the occultation. As remarked earlier, we have measured the entry angle for the occultation in question to be 35° before entry into the atmosphere. When defocusing is taken into account ($q^2 = 10$), the apparent entry angle becomes 81.9°. The frequency ν is mostly proportional to m. In Fig. 4, we show simulated radio scintillation power spectra for an apparent entry angle of 81.9°. We also show the log-amplitude power spectrum previously shown in Fig. 2b. We retain $v_s = 7.7$ km s^{-1} and $q^2 = 10$. First, we use $U_c = 1$ m s^{-1} and $H_c = 5$ km. We show the results for $\Delta = 5°$, 10°, and 20° because these bracket the data. No single value of Δ fits the data at all ν, however. The behavior of the simulations for substantially nonzero Δ does not change after implementation of the realistic value for the entry angle since the spacecraft appears to be crossing the wave phase fronts vertically in both cases.

In Fig. 5 we increase U_c to 3 m s^{-1} while retaining all the other parameters used in Fig. 4. The result is that the overall shape of the simulated spectra does not change but the overall amplitude does. That the overall amplitude increases seems contrary to our reasoning that the simulated scintillation spectrum reflects the saturated spectrum of gravity waves. This saturated spectrum holds that upon integration of the temperature variance spectrum over horizontal wavenumbers k_x', k_y', the resultant spectrum in m is proportional to m^{-3}:

$$\iint dk_x'\, dk_y'\, \mathbf{B}_T(k_x', k_y', m; z) = \frac{\Gamma^2}{m^3},$$

where Γ is the difference between the lapse rate of the atmosphere and the adiabatic lapse rate. Scintillations, though, reflect an integral over only one of the wavenumbers. That is,

$$W_X(\nu) \propto \int dk_y'\, \mathbf{B}_T(k_x' = 0, k_y', m; z).$$

Thus, simulations are not a reproduction of the saturated spectrum, but they might give the same spectral behavior if the $k_x' = 0$ component of the spectrum were proportional to the integral of the spectrum over k_x'. This proportionality evidently is dependent on the value of U_c that we use. When U_c is increased, the $k_x' = 0$ component of the spectrum tends to grow with respect to the integral of the spectrum over k_x'. We speculate that this happens because a greater fraction of the waves can reach 60-km altitude when U_c is increased.

The scintillation simulations for $U_c = 0.2$ m s^{-1} yield significantly different results than for larger values of U_c. The simulations are shown in Fig. 6. These curves are nearly flat in comparison with the previous simulations. In this case, the wave forcing is so weak that the waves in the vertical wavenumber range of interest do not break; hence, the scintillation spectra do not show the effects of the saturated spectrum of breaking waves. Since the flatness of these simulated spectra is not consistent with the data, we know that the forcing must be more intense than $U_c = 0.2$ m s^{-1} (Fig. 6).

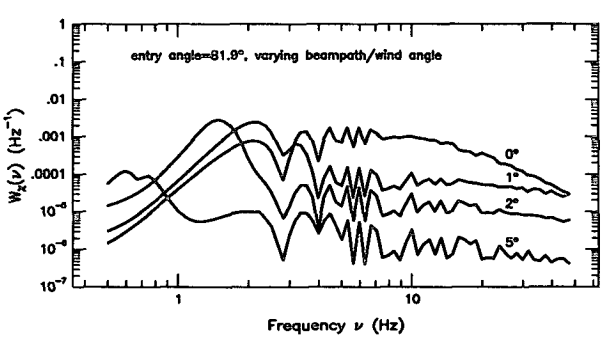

FIG. 6. Simulated scintillation spectra. The actual entry angle is 35°; the apparent entry angle is 81.9°. The gravity wave spectrum has $U_c = 0.2$ m s^{-1} and $H_c = 5$ km. The angle Δ is set to 0°, 1°, 2°, and 5°.

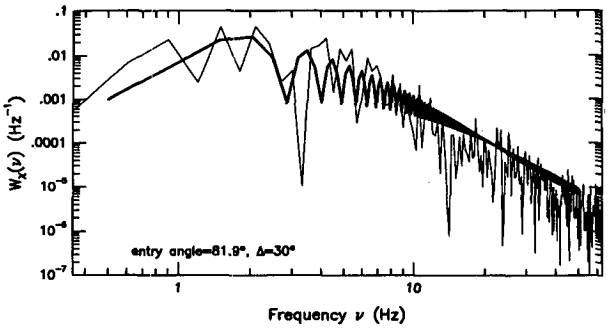

FIG. 7. Simulated scintillation spectrum with resolved fringes. In this simulated log-amplitude variance spectrum in frequency, we sample in ν more finely at high frequencies so that all of the fringes are resolved. We have set the entry angle to 81.9°, U_c to 3 m s^{-1}, H_c to 5 km, and the angle between the radio beam path and the winds Δ to 30°. The deemphasized curve is the data.

This flattening effect is not as obvious when $U_c = 1$ m s^{-1} (Fig. 4), and it is even less obvious when $U_c = 3$ m s^{-1} (Fig. 5). Since the simulations at $U_c = 3$ m s^{-1} show shapes more similar to the shape of the data, we can place a lower limit on U_c. We suggest a lower limit of 2 m s^{-1}.

We also require that Δ be large enough so that the dependence of $W_\chi(\nu)$ on ν is roughly proportional to ν^{-3} at high frequencies. In general, this occurs for Δ greater than 5°. Above this, while holding U_c fixed, the shape of the scintillations remains the same, but the overall amplitude decreases as Δ is increased. For example, when $U_c = 3$ m s^{-1}, we get a reasonable fit to the data for $\Delta \approx 30°$ (Fig. 5). If we increase the convective intensity U_c, then we would also have to increase Δ to get a reasonable fit. This implies that given a lower limit on U_c, we can also place a lower limit on Δ. We suggest that this lower limit on Δ is approximately 30°.

3) FRESNEL FRINGES

The dips that occur in the simulated scintillation spectra are fringes associated with Fresnel diffraction patterns. The first dip occurs near 3 Hz in Figs. 4 and 5. The second occurs near 4 Hz, etc. In weak scintillation theory for gravity waves, the fringes occur when the Fresnel filter function $\sin^2[\ldots]$ in Eq. (2) is nearly zero. Because $m^2/q^2 \gg k_x^2, k_y^2$ for gravity waves, the fringes are located at

$$\frac{m^2 a_f^2}{q^2} = n\pi, \tag{16a}$$

where n is a positive integer and $a_f^2 = R/2k$. We note that $2\pi\nu \approx m\dot{z}_a$ and that $\dot{z}_s = q^2\dot{z}_a$ to show that the sequence of frequencies ν_n at which there are fringes is

$$\nu_n = 2.813 \text{ Hz } \sqrt{n}. \tag{16b}$$

We have used a realistic value for the entry angle, 35°, and a spacecraft velocity of $v_s = 7.7$ km s^{-1}.

In most of the preceding scintillation simulations, the fringes are unresolved at high frequencies. In Fig. 7 we show a simulation in which all of the fringes between 0.5 and 50 Hz are resolved. We have used the same parameters used for Fig. 5, except $\Delta = 30°$. With this simulation, it is easier to see the general trend of the simulation, which matches the overall shape of the data more clearly than the previous simulations did. We do not expect that the fringes in this simulation and dips that occur in the data should line up, largely because the dips in the data are symptomatic of a single realization of a random process, not of a diffraction pattern.

4) VARYING THE BACKGROUND ATMOSPHERE

In this subsection we examine how different assumed mean states of the atmosphere affect the simulations. The actual stability profile $N^2(z)$ can be drawn from the occultation data itself. Woo and Armstrong (1980) give a value for N^2 that is consistent with the profile we have used for $N^2(z)$. Nevertheless, we vary the background stability structure so that we may know in the future how scintillations produced by gravity waves depend on the stability. Since the occultation occurred at such a high latitude, the mean state wind profile is not known. For this reason alone, we vary the background wind profile so that we may assess the validity of the conclusions we reached earlier.

First, we present simulated log-amplitude spectra for a different stability profile $N^2(z)$. We use a new profile for the Brunt–Väisälä frequency in which we have only decreased the peak value of N^2 by a factor of 2. The new profile is shown in Fig. 8. The slopes in the zonal wind profile have been adjusted so that Kelvin–Helmholtz instabilities are avoided (the Richardson number is always greater than 1/4). The net effect of this adjustment is only a 3 m s^{-1} westward shift to the winds

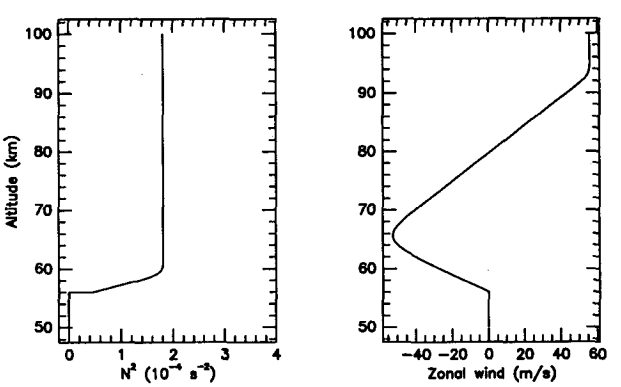

FIG. 8. Modified background stability. This is a modified version of the background atmosphere used in LI1. The peak N^2 has been decreased by a factor of 2. The zonal wind has been modified so that the Richardson number nowhere exceeds 1/4.

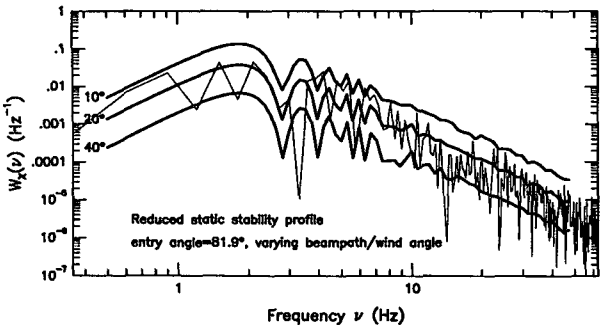

FIG. 9. Modified stability simulated scintillation spectra. These simulations utilize the reduced static stability profile shown in Fig. 8. The actual entry angle is 35°; the apparent entry angle is 81.9°. The gravity wave spectrum has $U_c = 3$ m s^{-1} and $H_c = 5$ km. The angle Δ is set to 10°, 20°, and 40°. The deemphasized curve is the data.

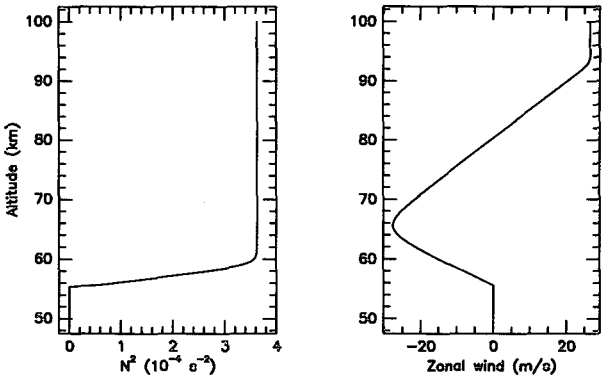

FIG. 10. Modified zonal winds. We plot the square of the Brunt–Väisälä frequency and the zonal wind versus altitude. The result is used to test the effect of changing the wind profile on the scintillation simulations. Compared to previous profiles of the winds, the shear above the convecting layer in this model has been reduced by a factor of 2. The background stability remains the same as in previous simulations.

above the convection. We have again set $U_c = 3$ m s^{-1} and we vary Δ. The result is Fig. 9.

The simulated scintillation spectra in Fig. 9 bear a strong resemblance to the previously computed spectra. Once again the slope above 10 Hz matches the slope of the power spectrum of the data. Also, the overall amplitude falls with increasing Δ and reaches a maximum for $\Delta \approx 5°$. When the static stability is reduced, the amplitude of the simulated spectra is also reduced (cf. Fig. 5). The reduction takes place because waves break at smaller amplitudes when the background atmosphere is less stable. Thus, the spectrum saturates at lower amplitudes of U_c when the stability is weaker, but the amplitude of U_c must be increased, or the angle Δ decreased, for a good match between the amplitude of the simulated scintillations and the data (Fig. 2b). This adjustment would be slight only because the stability is known to good accuracy a priori.

Next we present simulations for an altered background wind profile $\bar{u}(z)$. In the previously assumed profile, the wind differed by 55 m s^{-1} between the convecting layer and the zonal wind maximum at 67-km altitude. We reduce the shear above the convection by a factor of 2 so that the zonal wind differs by 28 m s^{-1} between the convecting layer and 67 km. Above the zonal wind maximum, the shear was also reduced by a factor of 2 so that the winds would still pass through zero at about 80-km altitude. The profiles of $N^2(z)$ and $\bar{u}(z)$ we use are plotted in Fig. 10. As before, we use $U_c = 3$ m s^{-1} and vary Δ. The result is Fig. 11.

In Fig. 11 we show simulations of the log-amplitude variance spectra in frequency. Decreasing the zonal wind shear increases the overall amplitude but does not change the shape of the simulated spectra. The shape is unchanged because the spectrum is saturated by wave breaking. The amplitude increases when wind shear decreases because fewer waves are absorbed at critical layers below 60 km, and thus the overall amplitude of the simulations increases.

The uncertainty in the zonal wind profile in polar latitudes affects the lower bound we place on the angle Δ between the winds and the radio beam but does not affect the lower bound we place on the convective intensity. Since the winds are most likely weaker than the wind profiles used in these simulations, the waves probably saturate for turbulent intensities U_c only slightly less than 3 m s^{-1}. On the other hand, since the simulations are greater in overall amplitude for the same values of Δ, it is possible that the lower limit placed on Δ may be too small. To maintain a reasonable fit to the data, larger values for Δ are required when the wind shear is decreased (cf. Fig. 5).

4. Discussion

We find that U_c must be at least 2 m s^{-1} so that the shape of the simulated spectra matches the shape of the

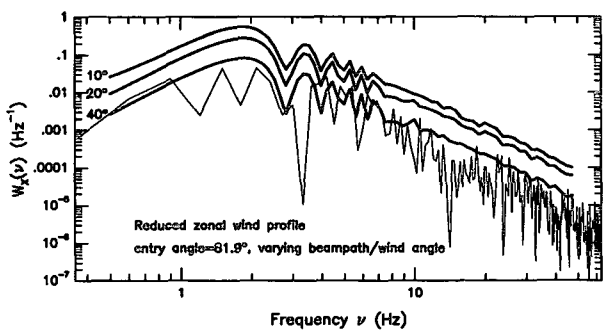

FIG. 11. Modified wind simulated scintillation spectra. We plot simulated log-amplitude variance simulations in which the entry angle is set to 81.9°. The gravity wave spectrum has $U_c = 3$ m s^{-1} and $H_c = 5$ km. The angle Δ is set to 10°, 20°, and 40°. We used the background profiles of stability and zonal wind illustrated in Fig. 10. The deemphasized curve is the data.

data. This limit on U_c has important consequences for Venus's atmosphere. Recall that the occultation data from which the scintillations in question were extracted comes from 86.6°N. The minimum value for U_c really represents a lower limit on the strength of the convection that generates the waves. The implication is that there is substantial dry convective activity in Venus's middle atmosphere even at polar latitudes. To date, there has been little effort placed in understanding polar atmospheric dynamics in Venus's atmosphere. That there is enough heat made available in the polar lower atmosphere of Venus so that middle atmospheric convection remains substantial is important. This could imply that the transport of heat in the lower atmosphere could extend to extremely high latitudes. This would not be possible if there were an isolated polar vortex, as is the case for the earth's southern winter. Thus, we suggest that there is considerable meridional mixing in Venus's lower atmosphere clear up to the North Pole.

The lower bound on the convective velocity variance permits placing a lower limit on the energy and momentum fluxes carried by the gravity waves emitted from the convection. We use a model of LI1 to calculate the amount of energy and momentum carried by gravity waves immediately after they break upon emission, given $U_c = 2\ \mathrm{m\ s^{-1}}$. We find that the lower bound on the eastward momentum flux is $1.26 \times 10^{-2}\ \mathrm{N\ m^{-2}}$, the westward momentum flux is $-2.59 \times 10^{-2}\ \mathrm{N\ m^{-2}}$, and the energy flux is $0.252\ \mathrm{W\ m^{-2}}$. This energy flux is a small fraction of the sensible heat transported within the convecting layer.

REFERENCES

Dewan, E. M., and R. E. Good, 1986: Saturation and the "universal" spectrum for vertical profiles of horizontal scalar winds in the atmosphere. *J. Geophys. Res.*, **91,** 2742–2748.

Essen, L., and K. D. Froome, 1951: The refractive indices and dielectric constants of air and its principal constituents at 24,000 Mc/s. *Proc. Roy. Soc. London, Ser. B,* **64,** 862–875.

Fjeldbo, G., A. Kliore, and V. R. Eshleman, 1971: The neutral atmosphere of Venus as studied with the Mariner V radio occultation experiments. *Astron. J.,* **76,** 123–140.

Geller, M. A., H. Tanaka, and D. C. Fritts, 1975: Production of turbulence in the vicinity of critical levels for internal gravity waves. *J. Atmos. Sci.,* **32,** 2125–2135.

Haugstad, B. S., 1979: Turbulence in planetary occultations. Part IV: Power spectra of phase and intensity fluctuations. *Icarus,* **37,** 322–335.

Hinson, D. P., and G. L. Tyler, 1983: Internal gravity waves in Titan's atmosphere observed by Voyager radio occultation. *Icarus,* **54,** 337–352.

——, and J. M. Jenkins, 1995: Magellan radio occultation measurements of atmospheric waves on Venus. *Icarus,* **114,** 310–327.

Ishimaru, A., 1973: A new approach to the problem of wave fluctuations in localized smoothly varying turbulence. *IEEE Trans. Antennas Propag.,* **21,** 47–53.

——, 1978: *Wave Propagation and Scattering in Random Media.* Vol. 1, *Single Scattering and Transport Theory,* Academic Press, 250 pp.

Jenkins, J. M., P. G. Steffes, D. P. Hinson, J. D. Twicken, and G. L. Tyler, 1994: Radio occultation studies of the Venus atmosphere with the Magellan spacecraft. Part II: Results from the October 1991 experiments. *Icarus,* **110,** 79–94.

Kliore, A. J., and I. R. Patel, 1980: Vertical structure of the atmosphere of Venus from Pioneer Venus orbiter radio occultations. *J. Geophys. Res.,* **85,** 7957–7962.

Leroy, S. S., 1995: Convectively generated internal gravity waves in Venus's middle atmosphere: Momentum transport and radio scintillations. Ph.D. thesis, California Institute of Technology, 204 pp.

——, and A. P. Ingersoll, 1994: Convective generation of gravity waves in Venus's atmosphere: Gravity wave spectrum and momentum transport, *J. Atmos. Sci.,* **52,** 3717–3737.

Sagdeev, R. Z., and Coauthors, 1986: Overview of VEGA Venus balloon in situ meteorological measurements. *Science,* **231,** 1411–1414.

Sato, T., and R. F. Woodman, 1982: Fine altitude resolution observations of stratospheric turbulent layers by the Arecibo 430 MHz radar. *J. Atmos. Sci.,* **39,** 2546–2552.

Seiff, A., D. B. Kirk, R. E. Young, R. C. Blanchard, J. T. Findlay, G. M. Kelly, and S. C. Sommer, 1980: Measurements of thermal structure and thermal contrasts in the atmosphere of Venus and related dynamical observations: Results from the four Pioneer Venus probes. *J. Geophys. Res.,* **85,** 7903–7933.

Smith, S. A., D. C. Fritts, and T. E. VanZandt, 1987: Evidence for a saturated spectrum of atmospheric gravity-waves. *J. Atmos. Sci.,* **44,** 1404–1410.

Tatarskii, V. I., 1961: *Wave Propagation in a Turbulent Medium.* McGraw Hill, 285 pp.

Timofeeva, T. S., O. I. Yakovlev, and A. I. Efimov, 1978: Radio wave fluctuation and turbulence of the nighttime Venusian atmosphere from radioscopy data of the space probe Venera 9. *Cosmic Res.,* **16,** 285–293.

Woo, R., 1975: Observations of turbulence in the atmosphere of Venus using Mariner 10 radio occultation measurements. *J. Atmos. Sci.,* **32,** 1084–1090.

——, and J. W. Armstrong, 1980: Radio occultation measurements of turbulence in the Venus atmosphere by Pioneer Venus. *J. Geophys. Res.,* **85,** 8031–8038.

——, and A. Ishimaru, 1981: Eddy diffusion coefficient for the atmosphere of Venus from radio scintillation measurements. *Nature,* **289,** 383–384.

——, ——, and W. B. Kendall, 1974: Observations of small scale turbulence in the atmosphere of Venus by Mariner 5. *J. Atmos. Sci.,* **31,** 1698–1706.

——, ——, and F. C. Yang, 1980: Radio scintillations during occultations by turbulent planetary atmospheres. *Radio Sci.,* **15,** 695–703.

Young, A. T., 1976: Scintillations during occultations by planets: Part I: An approximate theory. *Icarus,* **27,** 335–357.